Energy & Environmental Science

Partially Reduced Ru/RuO_2 Composites as Efficient and pH-Universal Electrocatalysts for Hydrogen Evolution

Journal:	*Energy & Environmental Science*
Manuscript ID	EE-ART-08-2021-002380
Article Type:	Paper
Date Submitted by the Author:	03-Aug-2021
Complete List of Authors:	Dang, Yanliu; University of Connecticut, Materials Science Wu, Tianli; Henan University Tan, Haiyan; University of Connecticut, Institute of Materials Science Wang, Jinlong; Wuhan University of Technology Cui, Can; University of Connecticut Kerns, Peter; University of Connecticut, Department of Chemistry Zhao, Wen; University of Connecticut Posada, Luisa; University of Connecticut Wen, Liaoyong; Westlake University, School of Engineering Suib, Steven; University of Connecticut, U-60, Department of Chemistry

Partially Reduced Ru/RuO_2 Composites as Efficient and pH-Universal Electrocatalysts for Hydrogen Evolution

Yanliu Dang,[a] Tianli Wu,[b] Haiyan Tan,[a] Jinlong Wang,[c] Can Cui,[a] Peter Kerns,[d] Wen Zhao,[a] Luisa Posada,[d] Liaoyong Wen,*[e] and Steven L. Suib,*[a,d]

a. Institute of Materials Science, U-3136, University of Connecticut, Storrs, Connecticut 06269, United States

b. Henan Key Laboratory of Photovoltaic Materials and School of Physics & Electronics, Henan University, Kaifeng 475004, China

c. School of Resources and Environmental Engineering, Wuhan University of Technology, Wuhan 430070, China

d. Department of Chemistry, U-3060, University of Connecticut, Storrs, Connecticut 06269, United States

e. Key Laboratory of 3D Micro/nano Fabrication and Characterization of Zhejiang Province, School of Engineering, Westlake University, 18 Shilongshan Road, Hangzhou 310024, Zhejiang Province, China

Broader context

The severe dependence on burning fossil fuels has triggered the depletion of traditional energy and the jeopardization of Earth's ecosystems. Alternatively, hydrogen that processes the highest mass-energy density (120 MJ Kg^{-1}), is deemed as clean energy that can be stored, moved, and delivered efficiently. Water electrolysis with renewable solar and wind energy resources is a promising option for carbon-free hydrogen production. Though Platinum (Pt) is a well-known catalyst for electrical hydrogen evolution reaction (HER), the high cost and unsatisfactory performance in non-acidic media restrict its scalable commercialization. Here, distinctive ruthenium and ruthenium oxide (Ru/RuO_2) composites are proposed as superior HER catalysts according to density functional theory calculations, which are then synthesized by cost-effectively *in-situ* and/or thermal processes. The optimal Ru/RuO_2 composites outperform commercial Pt/C catalysts for HER in a wide range of non-acidic media and real seawater as well. The comprehensive analysis of theoretical calculations and experimental results illustrate the structure-HER performance relationships for the first time, which not only come up with an outstanding catalyst for overall water splitting but also pave roads for the exploration of new catalysts.

ARTICLE

Partially Reduced Ru/RuO_2 Composites as Efficient and pH-Universal Electrocatalysts for Hydrogen Evolution

Received 00th January 20xx,
Accepted 00th January 20xx

DOI: 10.1039/x0xx00000x

Yanliu Dang,[a] Tianli Wu,[b] Haiyan Tan,[a] Jinlong Wang,[c] Can Cui,[a] Peter Kerns,[d] Wen Zhao,[a] Luisa Posada,[d] Liaoyong Wen,*[e] and Steven L. Suib,*[a,d]

Efficient and long-term stable electrocatalysts for the hydrogen evolution reaction (HER) via water splitting are urgently desired to ease the energy crisis and develop the sustainability of human society. However, the HER performance of state-of-the-art Pt in non-acidic solutions is unsatisfactory due to the severely sluggish kinetics. Here, DFT theoretical calculations reveal that the Ru/RuO_2 composites enable to pursue high HER activity under non-acidic conditions because of the distinctive Ru and RuO_2 interface, which possess not only a strong capability to adsorb and dissociate water but also appropriate binding energies of H and OH. Therefore, we employ a simple strategy, including heating under an oxygen-poor environment and/or *in-situ* electrochemical reduction, to partially reduce RuO_2. The formed Ru/RuO_2 interfaces demonstrate superior HER activities (e.g. η_{10}=17 mV, 35 mV dec^{-1} in 1 M KOH) than Pt (e.g. η_{10}=27 mV, 58 mV dec^{-1} in 1 M KOH) at both small (10 - 100 mA cm^{-2}) and large (1 A cm^{-2}) current densities in alkaline solution and even real seawater. Comprehensive experiments were conducted to investigate the structure-HER performance relationships. Moreover, benefiting from the bifunctional character of RuO_2, a two-electrode system based on Ru/RuO_2 composites and RuO_2 exhibits the lowest cell voltage for water splitting in both 1 M KOH and 0.5 M H_2SO_4, respectively. A 300 h-stability test at 10 mA cm^{-2} without an obvious decay demonstrates the industrial prospects of the Ru/RuO_2 composites to generate green energy.

Introduction

Hydrogen (H_2) is a promising candidate for the future energy supply because it has the highest gravimetric energy density of all fuels and water is the sole combustion product.[1,2] The conversion of abundant water into hydrogen motivates great interest in the electrolysis of water, which involves two half-reactions: the cathodic hydrogen evolution reaction (HER) and the anodic oxygen evolution reaction (OER).[3,4] To produce H_2 cost-effectively and sustainably, the desirable HER catalysts have to be both active and stable in acidic, alkaline, and neutral media.[5,6] Among reported electrocatalysts, Pt and Pt-group metals are the most efficient catalysts for the HER in acidic media due to the optimal Gibbs free energy (ΔG_H) of metal–hydrogen bonding (M-H_{ads}) at the center of the HER volcano plot.[7,8] However, producing H_2 in alkaline and neutral media remains a challenge due to the large kinetic energy barrier of the water dissociation step (i.e., the Volmer reaction)[9,10] and even the state-of-the-art Pt catalyst shows poor activity under those conditions.[11] Therefore, identifying efficient and economical HER catalysts functional in non-acidic environments, like seawater, is crucial to the hydrogen economy.[12]

Recently, many low-cost transition metal composites (oxides,[13] sulfides,[14,15] phosphides,[16–18] carbides,[19,20] and nitrides[21]) and carbon materials have been explored as alternatives in non-acidic media. However, their HER performance is still inferior to Pt-group materials, and also their catalytic and chemical stability do not meet the requirement of industrial applications and the environment.[22,23] On the other hand, Ruthenium (Ru), possessing a similar M–H_{ads} bond energy as Pt but with a cheaper price, shows a great potential to be an alternative HER catalyst.[24] Therefore, a few studies based on Ru metal, alloys, and composites have been tried,[25–37] such as RuCu nanocrystals,[38] carbon quantum dots (CQDs)-loaded Ru metal or RuNi bimetal nanoparticle electrocatalyst (Ru@CQDs, RuNi@CQDs),[28,35] Ru-Co nanoalloys,[33] and $Ru@C_2N$.[29,30] Some demonstrated high activity for the HER, attributed to their optimal hydrogen binding energy at the catalyst surface that is facilitated by either the formed alloy structure or the carbon substrates. However, these synthetic methods are complicated and have high-energy consumption, like the synthesis of CQDs supports, metal-organic frameworks (MOFs) precursors, and high-temperature annealing processes.[30,39,40] To simplify the industrial process and lower the cost, catalysts that could work

[a] Institute of Materials Science, U-3136, University of Connecticut, Storrs, Connecticut 06269, United States
[b] Henan Key Laboratory of Photovoltaic Materials and School of Physics & Electronics, Henan University, Kaifeng 475004, China
[c] School of Resources and Environmental Engineering, Wuhan University of Technology, Wuhan 430070, China
[d] Department of Chemistry, U-3060, University of Connecticut, Storrs, Connecticut 06269, United States
[e] Key Laboratory of 3D Micro/nano Fabrication and Characterization of Zhejiang Province, School of Engineering, Westlake University, 18 Shilongshan Road, Hangzhou 310024, Zhejiang Province, China
Electronic Supplementary Information (ESI) available: [details of any supplementary information available should be included here]. See DOI: 10.1039/x0xx00000x

efficiently for the overall water-splitting reaction (both HER and OER) are especially preferred. Therefore, the development of facile processes to synthesize Ru-based catalysts with superior efficiency and bifunctional property for overall water-splitting are in demand.

To improve the HER performance of Ru-based catalysts, it is important to identify rate-limiting reaction steps. Various studies have illuminated the first step of water dissociation as well as proper M–H_{ads} bonds are the key issues.[41–43] Therefore, forming metal oxide/metal interfaces may be a method to improve the HER performance in non-acidic environments.[41] For example, Subbaraman et al. designed Li^+-Ni$(OH)_2$-Pt Interfaces for alkaline HER, which utilized the oxide to provide the active sites for water dissociation, while the metal to facilitate hydrogen adsorption and desorption to generate H_2.[44] Similar studies are also found for NiO/Ni-CNT and Ni/CeO2-CNT.[45,46] Moreover, consider that RuO_2 is the state-of-the-art catalyst for OER and displays great capability for water dissociation, but its electrocatalytic activity toward HER is not sufficient.[48,49] Hence, the formation of proper Ru/RuO_2 composites could be one of the simplest strategies to achieve cost-effective HER catalysts.

As the corresponding oxide of Ru, the phase transformation of RuO_2 into Ru inspired us to produce the Ru/RuO_2 composites via an *in-situ* electrochemical strategy. Understanding the electrochemical processing is crucial to control the transformation of RuO_2, however, the reduction of RuO_2 under negative potential is debated. It has been reported that $RuO(OH)_2$ is observed on the surface of RuO_2 and subsequently reduced to metallic Ru.[50] While the formation of metallic Ru has been doubted based on theoretical studies of shifts in the energy of the X-ray photoelectrons.[51] A more nuanced mechanism accounting for the pH of the reaction solution suggests that the reduction of RuO_2 only occurs in acidic media and not in alkaline solutions.[52] Therefore, conditions must be elucidated before implementing the electroreduction on RuO_2, which not only contribute to efficient catalyst design but also reveal the active sites.

Here, based on the guidance of density functional theory (DFT) calculations, we develop a simple method to precisely synthesize Ru/RuO_2 composites, which are capable of evolving H_2 with high efficiency and great stability in non-acidic media. Only small overpotentials are required to drive a current density of 10 mA cm^{-2} for HER in different conditions (η_{10} = 16, 17, 29 mV in 0.5 M H_2SO_4, 1 M KOH, and 1 M KPi, respectively), which are comparable to and even outperform the optimized commercial Pt/C and many other reported electrocatalysts. Systematic investigation reveals that the excellent HER performance is due to the synergistic effect of the Ru and RuO_2 interfaces, which could be obtained from the annealing under an oxygen-poor environment and/or *in-situ* electrochemical reduction. Further combining with the RuO_2 anode for overall water-splitting reaction, the Ru/RuO_2//RuO_2 two-electrode cell shows the best performance with great stability up to 300 h without noticeable degradation compared to the reported catalysts. Moreover, the Ru/RuO_2 composites not only outperform Pt/C in alkaline media from 10 to 1000 mA cm^{-2} with good stability but also in seawater as well. The study of structural changes and mechanisms of the HER of RuO_2 may provide further impetus for designing efficient and pH-universal water-splitting catalysts.

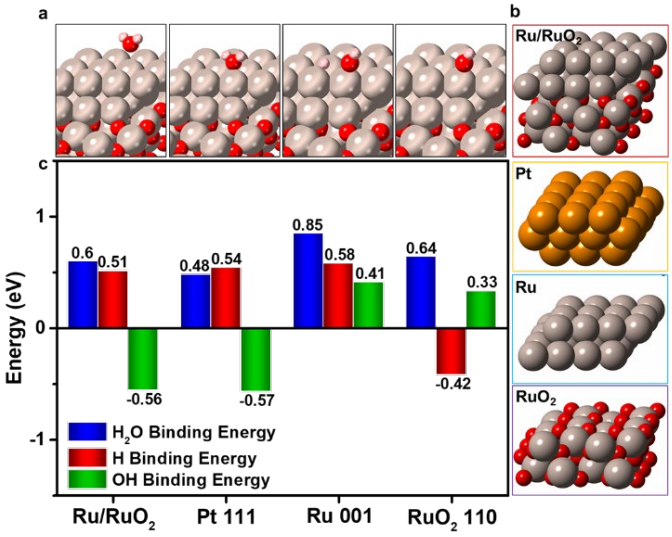

Figure 1. (a) Surface configuration of Ru/RuO_2 at different stages of the hydrogen evolution reaction. (b) Surface configuration of the four different catalysts used for the calculation (Ru/RuO_2, Pt, Ru, and RuO_2). (c) Theoretical calculation of binding energy on selected catalysts surface for H_2O, H and OH, respectively. Gold, grey, red, and pink balls represent platinum, ruthenium, oxygen, and hydrogen atoms, respectively.

DFT calculations for catalyst design

DFT calculations were performed to help design high-efficient catalysts for the HER. In acidic conditions, the metal–hydrogen (M–H_{ads}) bond serves as a key part of the HER process. While in alkaline and neutral media, the water dissociation step, as well as the proper M–H_{ad} are both significant for HER performance, and they depend on how H_2O, H, and OH bond to the surface of the catalysts. RuO_2 has outstanding catalytic activity toward the OER, while poor performance for the HER. The proper modification of RuO_2 with HER active Ru would help to design an effective HER catalyst. Hence, binding energies of H_2O, H and OH and the H_2O dissociation on the Pt (111), Ru(001) facets, RuO_2 (110), and Ru/RuO_2 composites were examined (Figure 1). The computed surfaces were selected from the most commonly observed ones in both experimental and theoretical modeling studies. The first step is water (H_2O) adsorption on the surface of selected metals (M). Due to the excellent H_2O adsorption capacity of Ru (0.85 eV) and RuO_2 (0.64 eV), the Ru/RuO_2 surface displays higher M–H_2O binding energy (0.60 eV) than Pt/C (0.48 eV), which improves H_2O adsorption and accelerates the Volmer step. In the following step, H_2O is decomposed into H and OH, and the easier water dissociates, the more protons can be supplied and the faster the reaction should be. As shown in Figure S1, the H_2O dissociation on the surface of Ru/RuO_2 is much easier than that on the Pt/C surface, because RuO_2 shows the lowest H_2O dissociation energy and contributes to H_2O dissociation on the surface of Ru/RuO_2. Furthermore, Ru/RuO_2 interface has moderate H and OH binding energies which are

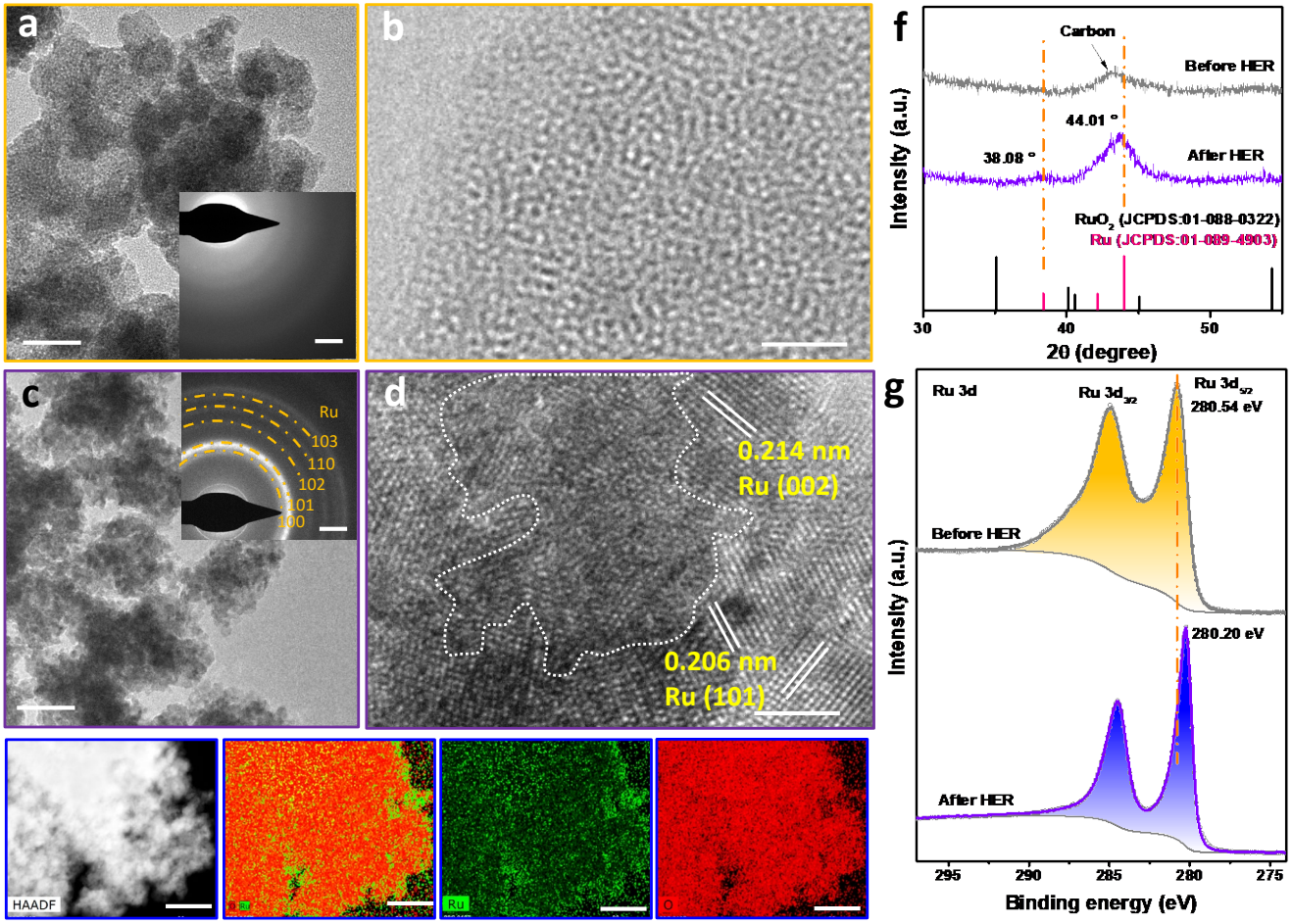

Figure 2. (a, b) Micrographs of as-obtained RuO2-300Ar: TEM images and corresponding SAED pattern (a) and HRTEM images (b). (c, d, e) Micrographs of RuO2-300Ar post HER in 1 M KOH: TEM image and corresponding SAED pattern (c) and HRTEM images (d) and EDX elemental mappings of Ru, O (e). (f, g) XRD pattern (f) and high-resolution Ru 3d XPS spectra (g) of RuO2-300Ar prior to and post HER in 1 M KOH. Scale bar: a, c 25 nm, 2 1/nm; b, d 2.5 nm; e 30 nm.

comparable to Pt/C, leading to efficient hydrogen evolution and rapid regeneration of active sites. Therefore, the Ru/RuO_2 composites demonstrate an outstanding H_2O adsorption, H_2O dissociation, and appropriate binding energies of H and OH, showing a potential HER catalyst to replace Pt in non-acidic media that is being carefully studied and correlated with detailed experiments.

Surface reduction chemistry and electrochemical evaluation

The catalyst was fabricated with a precipitation method followed by an annealing process. Potassium hydroxide (KOH) was used as the precipitant. After the introduction of KOH into the solution of $RuCl_3$, Ru^{3+} precipitated and formed RuO_2-RT($RuO_2{\cdot}xH_2O$, RT for short), which is also formulated as $Ru(OH)_3$. In terms of the heating process, the metal hydroxides are converted to metal oxides and are denoted as RuO_2-300Ar after annealing at 300 °C for 2 h under Ar atmosphere.

Transmission electron microscopy (TEM) and X-ray diffraction (XRD) were applied to investigate the morphology and crystal structure of obtained RuO_2-300Ar. The as-prepared RuO_2-300Ar materials are made of aggregated nanoparticles with a diameter of 50-100 nm (Figure 2a). The corresponding selected area electron diffraction (SAED) pattern in the inset of Figure 2a reveals a characteristic halo ring pattern due to an amorphous structure. Meanwhile, the high-resolution TEM (HRTEM) in Figure 2b shows a random distribution of atoms, which is consistent with the results of diffraction patterns in Figures 2a and 2f, indicating the amorphous structure of RuO_2-300Ar. Considering that there are many contradictory opinions regarding the structural changes of RuO_2 during the HER,[50–52] the structure and composition of RuO_2 are characterized after the HER experiments. Clearly, morphological changes and polycrystalline rings of hexagonal Ru are observed (Figure 2c). Meanwhile, the HRTEM image reveals an amorphous region and d-spacings of 0.214, 0.206 nm assigned to Ru (002), (101) facets, confirming the partial reduction of RuO_2 to Ru under negative potential (Figure 2d). Moreover, the energy-dispersive X-ray (EDX) spectroscopy analysis shows that most of the reduced Ru are distributed on the surface of the particles (Figure 2e). The diffraction pattern of materials after the HER exhibits two peaks located at 38.08 and 44.01° (Figure 2f), which are ascribed to (100) and (101) planes of crystalline Ru (JCPDS: 01-089-4903).

X-ray photoelectron spectroscopy (XPS) was performed to further examine the structural and electronic changes of the obtained RuO_2-300Ar, where the Ru $3d_{5/2}$ detected at 280.54 eV corresponds to Ru^{4+} before HER (Figure 2g). This peak shifts to a lower binding energy of 280.20 eV after HER, which is attributed to Ru^0. Raman was also carried out and the result shows three major Raman-active modes E_g, A_{1g}, B_{2g} of RuO_2 in both samples before and after HER (Figure S2), suggesting that RuO_2 still exists after HER. All these findings confirm that the amorphous RuO_2-300Ar was partially converted to Ru after HER and the mixture of Ru/RuO_2 composites serves as the catalytic component for producing hydrogen. A detailed study about structural changes of RuO_2 during HER will be discussed later.

To evaluate the catalytic activity during the HER, polarization curves are collected in 1 M KOH (pH = 14) with a three-electrode system, where the resistance compensation and RHE calibration of the reference electrode were applied to eliminate the effect of solution resistance and calculation errors of the reference electrode (Figure S3). Among the three commercial catalysts (Figure 3a), Pt/C still exhibits better activity for HER (27 mV) than Ru (32 mV), and commercial RuO_2 (100 mV) to drive a current density of 10 mA cm^{-2} (η_{10}). Noticeably, the RuO_2-300Ar electrode shows a η_{10} value of only 17 mV, which is even lower than that of the commercial Pt/C catalyst. Similar results are obtained with the rotating disk electrode (RDE) system (Figure S4).

To better understand the intrinsic and kinetic properties of catalysts, electrochemical surface area (ECSA) normalized polarization curves, charge transfer resistance, and Tafel slopes are calculated. The ECSA corrected RuO_2-300Ar electrode displays the highest HER activity, which is about 2.5 times that of Pt/C and Ru, and 17.7 times that of commercial RuO_2 at an overpotential of 80 mV (Figure S5, Table S1), suggesting the high intrinsic activity of RuO_2-300Ar toward HER. Electrochemical impedance spectroscopy (EIS) data show a smaller charge transfer resistance of RuO_2-300Ar (0.4 ohms) than that of Pt/C (2.9 ohms) at an overpotential of 50 mV for the HER, demonstrating more efficient electron transfer at the interface of the RuO_2-300Ar electrode and the electrolyte (Figure S6). Importantly, the Tafel slope of the RuO_2-300Ar electrode is 35 mV dec^{-1}, which is lower than that of Pt/C (59 mV dec^{-1}) and Ru (74 mV dec^{-1}) and commercial RuO_2 (101 mV dec^{-1}) in 1 M KOH solution (Figure 3b). Based on our knowledge, the overpotential and Tafel slope of RuO_2-300Ar outperforms most of the reported catalysts toward the HER (Figure 3c, Table S9).[53–57]

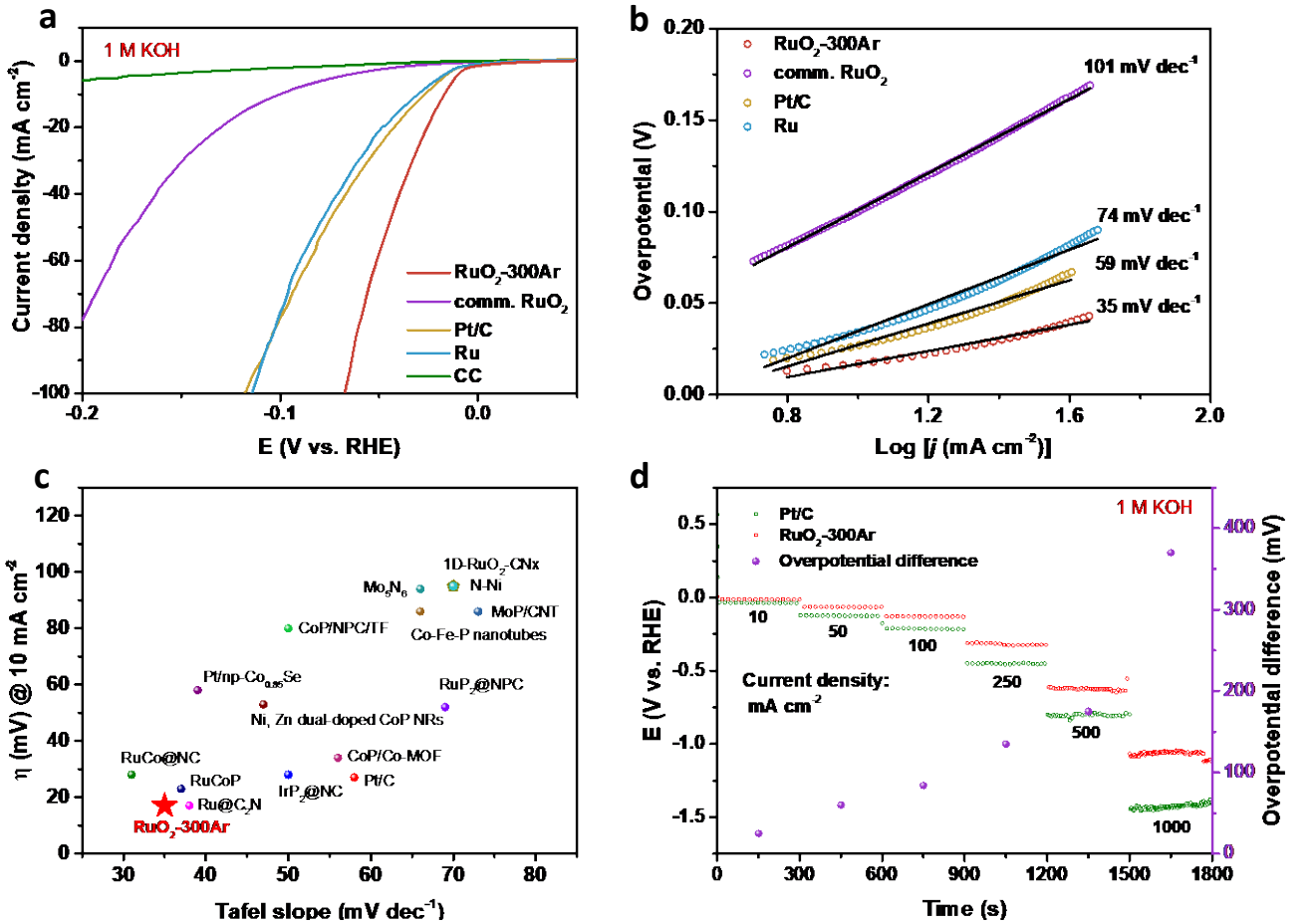

Figure 3. (a) Polarization curves of bare CC, Ru, Pt/C, commercial RuO_2, and RuO_2-300Ar in 1 M KOH. (b) Tafel plots of Ru, Pt/C, commercial RuO_2, and RuO_2-300Ar electrodes derived from (a). (c) Overpotentials and tafel slops of RuO_2-300Ar and Pt/C at 10 mA cm^{-2}, with other recently reported HER electrocatalysts in 1 M KOH. (d) Multi-current chronopotentiometric curves obtained with the RuO_2-300Ar and Pt/C electrodes in 1 M KOH without iR compensation.

Furthermore, the lower Tafel slope value of the RuO_2-300Ar catalyst implies faster charger transfer kinetics and a more rapid increase of current density for the HER with increasing overpotential, resulting in a competitive advantage for industrial applications, especially for current densities on the order of 1000 mA cm^{-2}. Hence, catalytic activity to drive current density up to 1000 mA cm^{-2} is compared between RuO_2-300Ar and commercial Pt/C without iR compensation to mimic the production of hydrogen in an electrolyzer. As shown in Figure 3d, RuO_2-300Ar surpasses Pt/C at all current densities from 10 to 1000 mA cm^{-2}. The difference of overpotential increases along with the increase of current density, and a 375 mV value of lower overpotential at 1000 mA cm^{-2} is observed for RuO_2-300Ar than that of Pt/C. In addition, the stabilities of RuO_2-300Ar under multiple current densities are also superior to that of Pt/C (Figure S7).

On another hand, in acidic conditions, the hydronium cation (H_3O^+) serving as the proton source is coupled with an electron transferred from the electrode to form adsorbed hydrogen atoms. An appropriate M–H_{ads} binding energy is important for HER under acidic conditions, which should be neither too low nor too high.[32] Pt is reported to show an optimal value of M-H_{ads}.[47] Surprisingly, the RuO_2-300Ar electrode merely requires a η_{10} value of 16 mV in 0.5 M H_2SO_4, comparable to that of the optimal Pt/C (Figure S8a). More importantly, a neutral solution (such as KPi) is environmentally friendly for water splitting, which not only reduces adverse damage to the environment but also extends the lifetime of devices.[58] Thus, the HER performance in 1 M KPi buffer electrolyte (pH=7) was

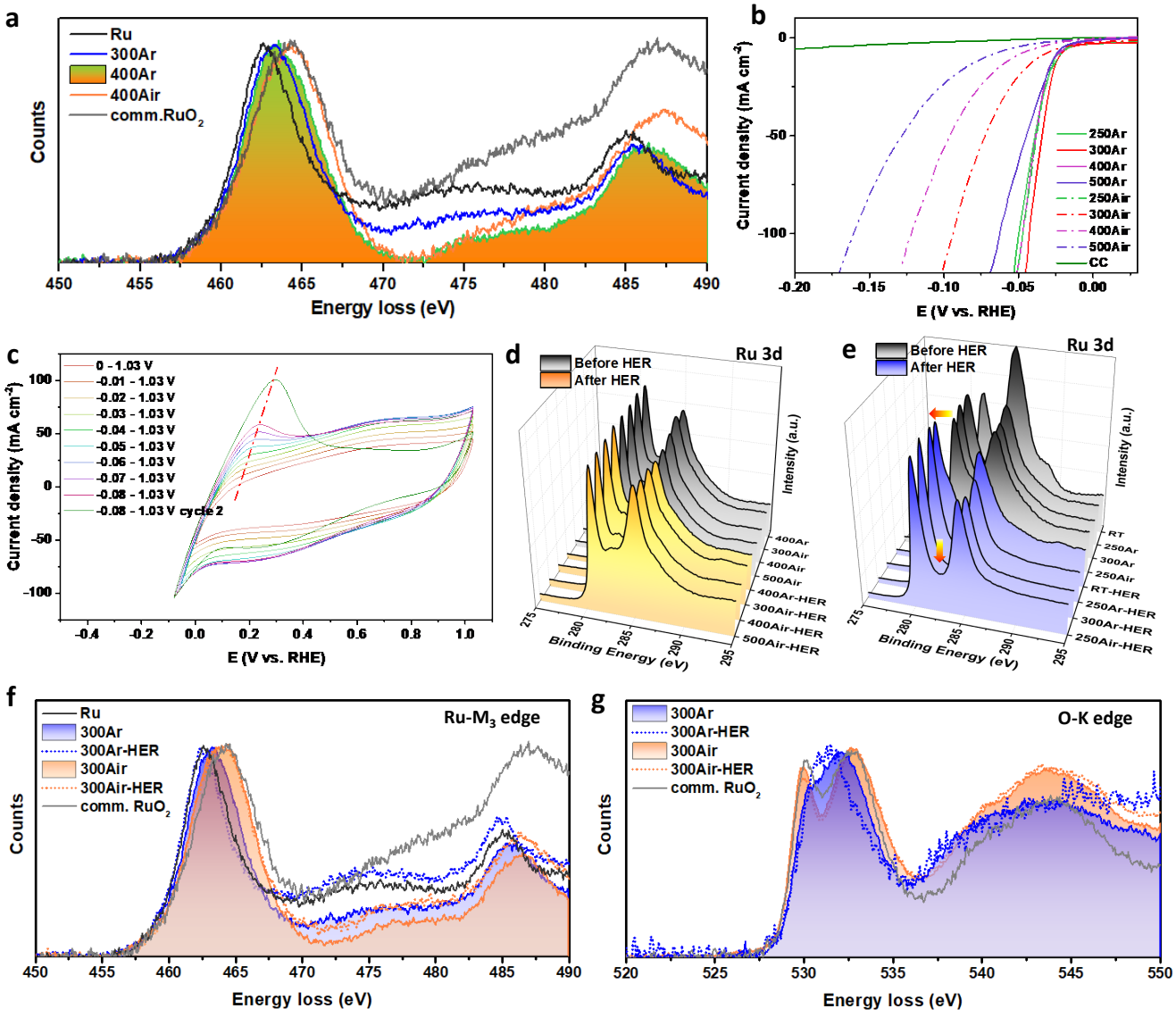

Figure 4. (a) Ru-M_3 edge EELS spectra of RuO_2-400Ar, 300Ar, 400Air, commercial Ru, and RuO_2. (b) Polarization of RuO_2 annealed under Ar and air in 1 M KOH. (c) Cyclic voltammogram study of RuO_2-300Ar in 1 M KOH: CV scan positively from x to 1.03 V vs. RHE without any activation to investigate the reduction process. -0.08 – 1.03 V cycle 2 is CV after holding the electrode at the potential of -0.08 V for 5 mins for HER. (d, e) High-resolution Ru 3d XPS spectra of crystallized RuO_2 materials (d) and amorphous RuO_2 materials (e) prior to and post HER in 1 M KOH. (f, g) Ru-M_3 edge (f) and O-K edge (g) EELS spectra of RuO_2-300Ar, 300Air prior to and post HER and compared with commercial Ru and RuO_2.

investigated. The RuO_2-300Ar electrode is also highly active and requires a η_{10} value of 29 mV (Figure S8b). The result is much better than most of the reported top-performing HER catalysts in neutral media (Table S11), for example, RuP_2@NPC (η_{10}=57 mV),[59] CrOx/Cu–Ni (η_{10}=48 mV),[42] Rh_2P (η_{10}=38 mV)[60] and Co-Fe-P (η_{10}=138 mV).[61]

Effect of annealing temperature and environment

To better understand the effect of annealing temperature and environment, various RuO_2 samples were obtained by treating RuO_2-RT at multiple temperatures and environments. Generally, low-temperature annealed RuO_2 materials are amorphous particles (Figure S9). As the temperature increases, diffraction peaks, which can be assigned to the tetragonal phase RuO_2 (JCPDS No. 01-088-0322), are present. Moreover, hexagonal close-packed Ru (JCPDS No. 01-089-4903) is observed in RuO_2-500Ar, due to the oxygen-poor environment. No Ru phase is present in RuO_2-500Air, due to the oxygen-rich surroundings during the calcination process in air. In-depth analyses from EELS reveal the oxidation state of bulk RuO_2 materials. Unlike the identical M_3 edge of 400Air and commercial RuO_2 (Figure 4a), the M_3 edge of 400Ar lies between that of Ru and RuO_2 references and shifts to a higher energy than that of 300Ar, suggesting that the samples heated under Ar have lower oxidation states due to oxygen-poor conditions. Notably, the surface areas are almost the same for the RuO_2 samples under Ar or Air at the same temperature (Figure S12). The detailed analyses for RuO_2 materials are presented in the Supporting Information(Figure S10-S12).

The electrocatalytic activities of RuO_2 samples were then carefully evaluated and compared (Figure 4b, S13, and Table S2). Based on these results, three features need to emphasize. Firstly, low-temperature annealed RuO_2 displays a higher HER activity regardless of Ar or air environment. Secondly, despite a similar ECSA for RuO_2-Air and RuO_2-Ar at each temperature, the HER performance of RuO_2-Ar is obviously superior to that of RuO_2-Air except at 250 °C. Thirdly, the ECSA trends of 300Ar $\approx$ 300Air > 300H_2 > 400Ar are not consistent with the HER activities of 300Ar $\approx$ 400Ar > 300Air $\approx$ 300H_2. Therefore, the HER performances are partially related to the annealing temperature and environment. Whereas the activity difference between RuO_2-Ar and RuO_2-Air is not related to the number of active sites but may be due to the generation of metallic or lower oxidation states Ru, which can be observed in the original structure of RuO_2-500Ar and 400Ar, as well as in the reduced RuO_2-300Ar after the HER. In addition, compared to the stable and high HER activity of RuO_2-300Ar, RuO_2-RT shows a progressively optimized HER performance with LSV test cycles (Figure S14). Hence, the structural transformations under negative potential need to be further studied to understand structure-HER performance relationships.

Effect of *in-situ* electrochemical reduction

First of all, the reduction process of RuO_2-300Ar was studied via multiple cyclic voltammogram (CV) scans positively from *x* V to 1.03 V *vs.* RHE. The initial *x* value is 0 and declines to -0.08 V with a decrease of 10 mV per scan. Unlike the initial CV having a rectangular shape which is a feature of RuO_2, the peak for hydrogen oxidation becomes apparent as the scanned potential shifts negatively (Figure 4c). After the chronoamperometry at -0.08 V for 5 mins, the CV curve shows a characteristic shape that is very similar to that of metallic Ru (Figure S15). It indicated that the negative potential enhances the reduction process within a few minutes or even seconds to form Ru metal, which will be analyzed via various techniques.

Post characterization of RuO_2 samples after HER was conducted. The morphology of RuO_2 at all temperatures seems unchanged after the HER based on SEM images (Figure S16). Unlike the crystallized RuO_2 maintaining almost an identical morphology and diffraction pattern (Figures S17, S18), Ru metal appears after HER on the amorphous RuO_2 samples (Figures S17, S19). Furthermore, the HRTEM images reveal that the newly formed lattices of Ru integrate with the irregular atomic arrangement, demonstrating the complexity of metallic Ru and substrate RuO_2. The composition and elemental ratios were also evaluated with EDX for each sample (Table S3, 4), indicating that oxygen atoms are losing after HER on the amorphous RuO_2 samples. The surface analyses from the XPS spectra and in-depth analyses from EELS on the Ru valence state reveal that the oxidation states of crystallized RuO_2 do not change post the HER (Figures 4d, f, S20). Notably, the shift of the Ru 3d region to lower binding energy for Ru^0 for the amorphous RuO_2 (Figures 4e, S21) and another shift of the M_3 edge to the direction of the Ru reference was observed for 300Ar after the HER (Figure 4f), indicating the reduction of amorphous RuO_2 under negative potential. The ratio of Ru to RuO_2 after the reduction was also determined by XPS spectra (Tables S5, S6), where the 300Ar sample after HER demonstrated a higher Ru to RuO_2 ratio of 4:1 than other samples. Furthermore, the single broad O-K edge of the 300Ar sample after HER is distinguished from the double peaks of the RuO_2 samples, confirming the reduction to metallic Ru (Figure 4g).

Comprehensive analyses of different samples show that the Ru/RuO_2 composites can be obtained by not only electroreduction but also thermal annealing under oxygen-poor environments. ECSA normalized polarization curves confirmed the superior intrinsic activity of Ru/RuO_2 composites toward HER (Figure S22) when comparing RuO_2-300Ar (Ru/RuO_2) to 300H_2 (Ru) and 300Air (RuO_2). According to the DFT calculations, RuO_2 is good at the first step-water dissociation but poor for H desorption whereas Ru does the opposite. Ru/RuO_2 not only benefits from RuO_2 to facilitate the water dissociation but also possesses optimal H binding energy to produce H_2 thanks to the existence of Ru, which further makes Ru/RuO_2 outperform commercial Pt/C, Ru, and RuO_2 for HER. Therefore, both the theoretical DFT and the experimental results about the Ru/RuO_2 composites kept consistent and successfully illustrated the HER mechanisms under acidic and alkaline conditions.

The application for overall water-splitting

RuO_2 has been a well-known and outstanding electrocatalyst for OER due to the great capability toward water dissociation and lower energy gaps of intermediates (*OO*H phase) during OER.[62] Materials that serve as bifunctional catalysts for both HER and OER are preferred for industrial applications, which could simplify these systems and reduce manufacturing costs.[63,64] Therefore, the overall water-splitting performance based on RuO_2 was investigated. Ru metal is not stable under OER conditions due to the oxidation of Ru^0 to dissolvable oxide Ru^{6+}.[62,65] While crystallized RuO_2 annealed in air displayed excellent stability and activity for the OER, where the RuO_2-300Air shows the best OER performance compared with RuO_2-400Air and commercial RuO_2 due to the smaller particle size and lower crystallization (Figures S23 and S24). Hence, RuO_2-300Air was used as the counter electrode for OER and paired with RuO_2-300Ar to drive the overall water-splitting reaction. In both alkaline and acidic media (Figure 5a), only 1.45 and 1.54 V are required for 10 and 100 mA cm^{-2}, respectively, which is comparable to reported catalysts (Table S12).[54,56,63,66,67] Long-term stability tests based on two electrode of RuO_2-300Ar//RuO_2-300Air were also collected (Figures 5b and S25). In either 1 M KOH or 0.5 M H_2SO_4 solution, RuO_2-300Ar//RuO_2-300Air maintains excellent catalytic activity for water splitting for up to 300 h. Even though the power was deliberately switched off for 24 h during the testing, the catalytic activity and stability of this system are almost unaffected, which is further confirmed by elemental analysis that no signal of Ru in the electrolyte after the usage.

In this work, we also studied the HER performance of the RuO_2-300Ar electrocatalyst in real seawater (Figure S26). A multi-step chronoamperometric curve was carried out to compare the HER performance of RuO_2-300Ar and Pt/C at different current densities from 10 to 250 mA cm^{-2} (Figure 5c). RuO_2-300Ar surpassed Pt/C at each current density and an overpotential difference of 198 mV was observed when driving 250 mA cm^{-2}. The overall water-splitting performance was also compared with the two-electrode configuration between RuO_2-300Ar//RuO_2-300Air and Pt/C//comm. RuO_2 (Figure 5d), and the set-up photo and video for water-splitting in real seawater are shown in Figure 5e and Supporting Information (video). The potential required for RuO_2-300Ar//RuO_2-300Air was 203 mV lower than that of Pt/C//comm. RuO_2 to produce 100 mA cm^{-2}, where its advantages became obvious with the increase of current density.

Conclusions

In summary, under the guidance of DFT calculations, unique Ru/RuO_2 composites were proposed and successfully obtained via simple heating under oxygen-poor environments and/or *in-situ* electrochemical reduction. The electrochemical evaluation of the Ru/RuO_2 composites displays comparable and even better HER activity than Pt/C and many other electrocatalysts at pH values from 0 to 14. Both the theoretical DFT and the

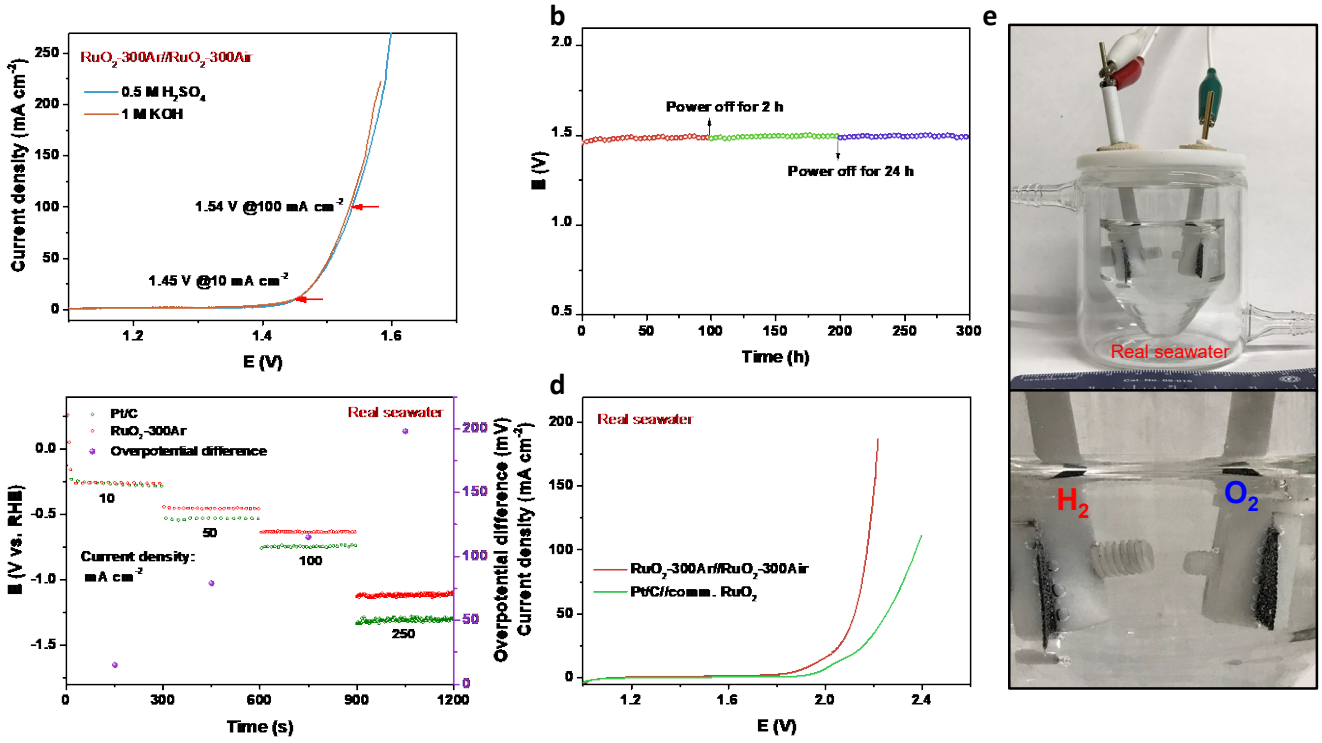

Figure 5. (a, b) Overall water-splitting of the electrolyzer RuO_2-300Ar//RuO_2-300Air: polarization curves in 0.5 M H_2SO_4 and 1 M KOH solution (a) and long-time stability test at 10 mA cm^{-2} in 1 M KOH (b). (c) Multi-current chronopotentiometric curves obtained with the RuO_2-300Ar and Pt/C electrode in real seawater without iR compensation. (d) Polarization curves for overall water-splitting of the electrolyzer RuO_2-300Ar//RuO_2-300Air in real seawater. (e) The two-electrode set-up of RuO_2-300Ar//RuO_2-300Air for overall water-splitting in real seawater.

experimental results illustrated that the origin of the excellent electrocatalysis is due to the synergistic effect of the Ru/RuO_2 interface, which holds outstanding H_2O adsorption, H_2O dissociation, and appropriate binding energies of H and OH. The two-electrode study shows that the RuO_2-300Ar//RuO_2-300Air system can be used as potential electrocatalysts for overall water-splitting in both acidic and alkaline electrolytes and even in real seawater, which provides a promising entry point for serving as catalysts for commercial water electrolyzers. Our work proposes a novel cost-effective strategy to realize metal/metal oxide catalysts that are highly active and stable for generating hydrogen under pH-universal electrolytes.

Experimental

Chemicals. Ruthenium (III) chloride hydrate ($RuCl_3 \cdot xH_2O$, Sigma-Aldrich), potassium hydroxide (KOH, Sigma-Aldrich), Ruthenium black (particle size:6nm, Sigma-Aldrich), 20% Pt/C (20% Pt on graphite, Sigma-Aldrich), Nafion solution (5 wt. % in a mixture of alcohols and water, Fuel Cell Store), carbon (Vulcan XC-72) were used as received. Carbon Cloth (CC) was purchased from Fuel Cell Store and cleaned with water, ethanol, and acetone before use.

Synthesis of RuO_2. RuO_2 was synthesized by a simple solution method and followed by annealing in different atmospheric conditions. In a typical synthesis, 100 mg of $RuCl_3 \cdot xH_2O$ was dissolved in 10 mL of distilled deionized water (DDW) with magnetic stirring, forming an acidic solution. Then 1 M KOH solution was dropwise added into the solution while stirring. The reaction was done when the pH of the solution was close to 7. After the reaction, the product was decanted and rinsed with DDW five times using a centrifuge and dried in a vacuum oven at 60 °C overnight. The as-prepared sample is denoted as RuO_2-RT (RT for short). The obtained precursors were then annealed at 250, 300, 400, 500 °C for 2 h under Ar atmosphere with a ramping rate of 5 °C/min to form RuO_2-250Ar, RuO_2-300Ar, RuO_2-400Ar, RuO_2-500Ar, respectively (250Ar, 300Ar, 400Ar, 500Ar for short). For comparison, the obtained products were calcined under Air atmosphere with the same program to prepare RuO_2-250Air, RuO_2-300Air, RuO_2-400Air, RuO_2-500Air, respectively (250Air, 300Air, 400Air, 500Air for short). To obtain Ru, the precursors were calcined at 300 °C for 2 h under H_2 atmosphere.

Preparation of pure RuO_2 electrode. About 10 mg of RuO_2 catalyst was dispersed in 500 µL of a water/ethanol mixture with a volume ratio of 1:1. The suspension was ultrasonicated for 30 min. Then 100 µL of the homogeneous suspension was dropped onto cleaned CC and left to dry under air. The active loading of the catalysts was 2 mg cm^{-2}. For simplicity, these pure RuO_2 electrodes were named according to the annealing temperature and atmosphere, such as RT, 250Ar, 300Ar, 400Ar, 500Ar, 250Air, 300Air, 400Air, and 500Air. After electrochemical measurements, these coated CCs were placed in a vial and ultrasonicated to collect catalysts. The collected catalysts after HER are denoted as RT-HER, 250Ar-HER, 300Ar-HER, 400Ar-HER, 500Ar-HER, 250Air-HER, 300Air-HER, 400Air-HER, and 500Air-HER. Then samples were washed with DDW and dried in a vacuum oven at 60 °C overnight for further characterization.

Preparation of 20% RuO_2/C and 20% Ru/C electrodes. About 1 mg of RuO_2-300Ar, 4 mg of carbon (VulcanXC-72) and 40 µL of a 5 wt% Nafion solution were dispersed in 460 µL of a water/ethanol mixture with a volume ratio of 1:1. The suspension was ultrasonicated for 30 min. Then 100 µL of the homogeneous suspension was dropped onto washed CC and left to dry under air. The active loading of the catalyst RuO_2-300Ar was 0.2 mg cm^{-2}. To prepare the 20% Ru/C electrode, 1 mg of commercial Ru metal was used instead of RuO_2-300Ar, and other conditions were kept the same. The active loading of the Ru catalyst was 0.2 mg cm^{-2}.

Preparation of 20% Pt/C electrode. To prepare the 20% Pt/C electrode, 5 mg of commercial Pt/C was used instead of 1 mg of RuO_2-300Ar and 4 mg of carbon, and other conditions were maintained the same. The active loading of the catalyst Pt was 0.2 mg cm^{-2}.

Rotating Disk electrode. About 1 mg of RuO_2-300Ar, 4 mg of carbon (VulcanXC-72) and 40 µL of a 5 wt% Nafion solution were dispersed in 960 µL of a water/ethanol mixture with a volume ratio of 1:1. The suspension was ultrasonicated for 30 min. Then 8 µL of the homogeneous suspension was dropped onto polished graphite (surface area 0.196 cm^2) and left to dry under air. The active loading of the RuO_2-300Ar catalyst was 0.04 mg cm^{-2}. For Pt/C, 5 mg of 20% Pt/C was dispersed instead of RuO_2-300Ar and carbon. The active loading amount is the same as RuO_2-300Ar.

Material Characterization. The X-ray diffraction (XRD) experiments were performed using a Rigaku Ultima IV diffractometer (Cu Kα radiation, λ = 0.15406 nm) at a beam voltage of 40 kV and a current of 44 mA. Due to the limited amount of material after HER, the XRD patterns were compared by collecting the data of working electrodes (catalysts coated carbon cloth). The peak at 43° is attributed to the substrate carbon cloth. The Raman spectra were taken on a Renishaw 2000 Raman microscope, which includes an optical microscope and a CCD camera for multichannel detection. A laser of 514 nm was used as the excitation source and silicon wafer was used to calibrate the instrument. The morphologies of the materials were investigated using scanning electron microscopy (SEM) (FEI Nova SEM 450) with an accelerating voltage of 2.0 kV. Energy-dispersive X-ray spectroscopy (EDX) was collected on an Oxford Aztec energy microanalysis system with X-Max 80 silicon drift detector. Detailed information of the surface morphology, particle size, and structure were performed via transmission electron microscopy (TEM) using a Talos F200X instrument with an accelerating voltage of 200 kV. X-ray photoelectron spectroscopy (XPS) measurements were done on a PHI Model 590 spectrometer with multiprobes (Al Kα radiation, λ = 1486.6 eV, operated at 250 W). The energy calibration was referenced to the C 1s peak at 284.8 eV during analysis. The surface area of the material was determined by using the Brunauer-Emmett-Teller (BET) method on a Quantachrome Autosorb-1-1C automated adsorption system. Electron energy loss spectroscopy (EELS) was acquired with a Themis instrument in the 300 kV TEM diffraction mode with a convergence angle of

about 1 mrad and a collection angle of about 2.5mrad. Elemental compositions of the electrolyte before and after the HER were determined by X-ray fluorescence (XRF) using a Rigaku ZSX Primus IV sequential wavelength-dispersive XRF diffractometer equipped with a 4 kW Rh anode X-ray tube.

Electrochemical Measurements. Electrochemical measurements were performed on a CHI 760E electrochemical workstation using a three-electrode configuration. The cell setup consisted of a working electrode coated with catalysts, a graphite rod as counter electrode, and Hg/HgO, KOH (1.0 M) reference electrode for measurements in 1.0 M KOH, Hg/Hg_5O_4, K_2SO_4(sat) reference electrode for measurements in 0.5M H_2SO_4, Saturated calomel electrode (SCE) for measurement in 1.0 M KPi. The reference electrodes were calibrated against a reversible hydrogen electrode in high purity hydrogen saturated solution using two Pt wires as the working and counter electrodes, respectively. The average of the potentials at which the current crossed zero was taken to be the thermodynamic potential for the hydrogen electrode reactions (Figure S3).

To study alterations in the electrochemical behavior of the catalysts, cyclic voltammetry (CV) in the potential range of 0 – 1.03 V vs. RHE was investigated before and after HER measurements. Linear sweep voltammetry (LSV) was measured at ambient temperature to evaluate the HER activity of the catalysts with a sweep rate of 2 mV s^{-1}. Before collecting the LSV curves, at least 20 cycles of CV in the active region were performed and continuous H_2 was purged into the electrolyte to establish standard conditions. A chronopotentiometric test was done to show electrode durability. A continuous current density of 10 mA cm^{-2} was used for the cathodic reaction without iR-compensation. The Tafel slopes were calculated by fitting the linear regions of the Tafel plots to the Tafel equation (Z=blog(j)+a) by replotting the polarization curves. Electrochemical impedance spectroscopy (EIS) was carried out in the potentiostatic mode with a frequency range from 0.1 to 100 kHz. To measure the ECSAs, the double-layer capacitance was measured using CV with a scan rate ranging from 5 to 50 mV s^{-1} in a non-Faradaic potential window of 0.5 to 0.6 V vs. RHE in 1 M KOH. A specific capacitance of 40 uF cm^{-2} was used to calculate the ECSAs for RuO_2, Ru, and Pt. All the LSV tests were represented with iR compensation except when noted, which is done via iR compensation command in CHI software by applying the test potential, step amplitude, compensation level and overshoot level as 0 V, 0.05 V, 100% and 2%, respectively.

DFT calculation

For DFT calculations, we used the Vienna Ab initio Simulation Package (VASP) to calculate the binding energy for the specific surfaces of materials.[70,71] The projected augmented wave pseudopotentials[72] and Perdew–Burke–Ernzerhof generalized gradient-corrected exchange-correlation potential[73] are implemented with the VASP package. A plane-wave basis using a planewave kinetic energy cutoff of 500 eV and gamma-centered Monkhorst–Pack30 electronic wavevector grid of 5 × 5 × 1 were applied for the calculations. First-order Methfessel–Paxton electron smearing of 0.05 eV and Spin-polarizations were considered in the DFT.

Conflicts of interest

There are no conflicts to declare.

Acknowledgements

The TEM studies were performed using the facilities in the UConn/Thermo Fisher Scientific Center for Advanced Microscopy and Materials Analysis (CAMMA). We thank the US Department of Energy, Office of Basic Energy Sciences, Division of Chemical, Biological and Geological Sciences under grant DE-FG02-86ER13622.A000 for support of this research. Dr. Wen acknowledge support from the National Natural Science Foundation of China (52003225) and Westlake Education Foundation.

References

1 M. G. Schultz, *Science.*, 2009, **624**, 624–628.
2 J. A. Turner, *Science.*, 2004, **305**, 972–975.
3 C. G. Morales-Guio, L. A. Stern and X. Hu, *Chem. Soc. Rev.*, 2014, **43**, 6555–6569.
4 Michael G. Walter, *Chem. Rev.*, 2010, **110**, 6446–6473.
5 S. Anantharaj, S. R. Ede, K. Sakthikumar, K. Karthick, S. Mishra and S. Kundu, *ACS Catal.*, 2016, **6**, 8069–8097.
6 C. Cui, X. Hu and L. Wen, *J. Semicond.*, 2020, **41**, 091705.
7 J. Zhang, Y. Zhao, X. Guo, C. Chen, C. L. Dong, R. S. Liu, C. P. Han, Y. Li, Y. Gogotsi and G. Wang, *Nat. Catal.*, 2018, **1**, 985–992.
8 S. Ye, F. Luo, Q. Zhang, P. Zhang, T. Xu, Q. Wang, D. He, L. Guo, Y. Zhang, C. He, X. Ouyang, M. Gu, J. Liu and X. Sun, *Energy Environ. Sci.*, 2019, **12**, 1000–1007.
9 R. Subbaraman, D. Tripkovic, K. C. Chang, D. Strmcnik, A. P. Paulikas, P. Hirunsit, M. Chan, J. Greeley, V. Stamenkovic and N. M. Markovic, *Nat. Mater.*, 2012, **11**, 550–557.
10 K. Lu, Y. Liu, F. Lin, I. A. Cordova, S. Gao, B. Li, B. Peng, H. Xu, J. Kaelin, D. Coliz, C. Wang, Y. Shao and Y. Cheng, *J. Am. Chem. Soc.*, 2020, **142**, 12613–12619.
11 I. Ledezma-Yanez, W. D. Z. Wallace, P. Sebastián-Pascual, V. Climent, J. M. Feliu and M. T. M. Koper, *Nat. Energy*, 2017, **2**, 1–7.
12 X. Lu, J. Pan, E. Lovell, T. H. Tan, Y. H. Ng and R. Amal, *Energy Environ. Sci.*, 2018, **11**, 1898–1910.
13 T. Kou, M. Chen, F. Wu, T. J. Smart, S. Wang, Y. Wu, Y. Zhang, S. Li, S. Lall, Z. Zhang, Y. S. Liu, J. Guo, G. Wang, Y. Ping and Y. Li, *Nat. Commun.*, 2020, **11**, 1–10.
14 K. J. H. Lim, G. Yilmaz, Y. F. Lim and G. W. Ho, *J. Mater. Chem. A*, 2018, **6**, 20491–20499.
15 X. Ren, W. Wang, R. Ge, S. Hao, F. Qu, G. Du, A. M. Asiri, Q. Wei, L. Chen and X. Sun, *Chem. Commun.*, 2017, **53**, 9000–9003.
16 J. F. Callejas, C. G. Read, C. W. Roske, N. S. Lewis and R. E. Schaak, *Chem. Mater.*, 2016, **28**, 6017–6044.
17 Y. Dang, J. He, T. Wu, L. Yu, P. Kerns, L. Wen, J. Ouyang and S. L. Suib, *ACS Appl. Mater. Interfaces*, 2019, **11**, 29879–29887.

18 L. Yu, J. Zhang, Y. Dang, J. He, Z. Tobin, P. Kerns, Y. Dou, Y. Jiang, Y. He and S. L. Suib, *ACS Catal.*, 2019, **9**, 6919–6928.

19 C. Chen, A. Wu, H. Yan, Y. Xiao, C. Tian and H. Fu, *Chem. Sci.*, 2018, **9**, 4746–4755.

20 C. Yang, R. Zhao, H. Xiang, J. Wu, W. Zhong, W. Li, Q. Zhang, N. Yang and X. Li, *Adv. Energy Mater.*, 2020, **10**, 2002260.

21 Y. Chen, J. Yu, J. Jia, F. Liu, Y. Zhang, G. Xiong, R. Zhang, R. Yang, D. Sun, H. Liu and W. Zhou, *Appl. Catal. B Environ.*, 2020, **272**, 118956.

22 A. Dutta and N. Pradhan, *J. Phys. Chem. Lett.*, 2017, **8**, 144–152.

23 J. Mahmood, M. A. R. Anjum, S. H. Shin, I. Ahmad, H. J. Noh, S. J. Kim, H. Y. Jeong, J. S. Lee and J. B. Baek, *Adv. Mater.*, 2018, **1805606**, 1–7.

24 W. J. Mitchell, J. Xie, T. A. Jachimowski and W. H. Weinberg, *J. Am. Chem. Soc.*, 1995, **117**, 2606–2617.

25 X. Qin, L. Zhang, G. Xu, S. Zhu, Q. Wang, M. Gu, X. Zhang, C. Sun, P. B. Balbuena, K. Amine and M. Shao, *ACS Catal.*, 2019, **9**, 9614–9621.

26 K. Li, Y. Li, Y. Wang, J. Ge, C. Liu and W. Xing, *Energy Environ. Sci.*, 2018, **11**, 1232–1239.

27 B. Lu, L. Guo, F. Wu, Y. Peng, J. E. Lu, T. J. Smart, N. Wang, Y. Z. Finfrock, D. Morris, P. Zhang, N. Li, P. Gao, Y. Ping and S. Chen, *Nat. Commun.*, 2019, **10**, 631.

28 Y. Liu, X. Li, Q. Zhang, W. Li, Y. Xie, H. Liu, L. Shang, Z. Liu, Z. Chen, L. Gu, Z. Tang, T. Zhang and S. Lu, *Angew. Chemie - Int. Ed.*, 2020, **59**, 1718–1726.

29 J. Wang, Z. Wei, S. Mao, H. Li and Y. Wang, *Energy Environ. Sci.*, 2018, **11**, 800–806.

30 J. Mahmood, F. Li, S. Jung, M. S. Okyay, I. Ahmad, S. Kim, N. Park, H. Y. Jeong and J. Baek, *Nat. Nanotechnol.*, 2017, **12**, 441–446.

31 J. Zhang, P. Liu, G. Wang, P. P. Zhang, X. D. Zhuang, M. W. Chen, I. M. Weidinger and X. L. Feng, *J. Mater. Chem. A*, 2017, **5**, 25314–25318.

32 Y. Zheng, Y. Jiao, Y. Zhu, L. H. Li, Y. Han, Y. Chen, M. Jaroniec and S. Z. Qiao, *J. Am. Chem. Soc.*, 2016, **138**, 16174–16181.

33 J. Su, Y. Yang, G. Xia, J. Chen, P. Jiang and Q. Chen, *Nat. Commun.*, 2017, **8**, 16028.

34 Y. Li, L. A. Zhang, Y. Qin, F. Chu, Y. Kong, Y. Tao, Y. Li, Y. Bu, D. Ding and M. Liu, *ACS Catal.*, 2018, **8**, 5714–5720.

35 W. Li, Y. Liu, M. Wu, X. Feng, S. A. T. Redfern, Y. Shang, X. Yong, T. Feng, K. Wu, Z. Liu, B. Li, Z. Chen, J. S. Tse and S. Lu, *Adv. Mater.*, 2018, **1800676**, 1–8.

36 C. Chen, D. Wu, Z. Li, R. Zhang, C. Kuai, X. Zhao, C. Dong, S. Qiao, H. Liu and X. Du, *Adv. Energy Mater.*, 2019, **1803913**, 1803913.

37 J. Xu, T. Liu, J. Li, B. Li, Y. Liu, B. Zhang, D. Xiong, I. Amorim, W. Li and L. Liu, *Energy Environ. Sci.*, 2018, **11**, 1819–1827.

38 D. Cao, J. Wang, H. Xu and D. Cheng, *Small*, 2020, **16**, 1–11.

39 Y. Xu, S. Yin, C. Li, K. Deng, H. Xue, X. Li, H. Wang and L. Wang, *J. Mater. Chem. A*, 2018, **6**, 1376–1381.

40 Y. L. Wu, X. Li, Y. S. Wei, Z. Fu, W. Wei, X. T. Wu, Q. L. Zhu and Q. Xu, *Adv. Mater.*, 2021, **2006965**, 1–12.

41 X. Tian, P. Zhao and W. Sheng, *Adv. Mater.*, 2019, **1808066**, 1808066.

42 C.-T. Dinh, A. Jain, F. P. G. de Arquer, P. De Luna, J. Li, N. Wang, X. Zheng, J. Cai, B. Z. Gregory, O. Voznyy, B. Zhang, M. Liu, D. Sinton, E. J. Crumlin and E. H. Sargent, *Nat. Energy*, 2018, **4**, 107–114.

43 N. Mahmood, Y. Yao, J. W. Zhang, L. Pan, X. Zhang and J. J. Zou, *Adv. Sci.*, 2018, **5**, 1700464.

44 R. Subbaraman, D. Tripkovic, D. Strmcnik, K. C. Chang, M. Uchimura, A. P. Paulikas, V. Stamenkovic and N. M. Markovic, *Science.*, 2011, **334**, 1256–1260.

45 M. Gong, W. Zhou, M. Tsai, J. Zhou, M. Guan, M. Lin, B. Zhang, Y. Hu, D. Wang, J. Yang, S. J. Pennycook, B. Hwang and H. Dai, *Nat. Commun.*, 2014, **5**, 1–6.

46 Z. Weng, W. Liu, L. Yin, R. Fang, M. Li, I. Altman, Q. Fan, F. Li, H. Cheng and H. Wang, *Nano Lett.*, 2015, **15**, 7704–7710.

47 Z. W. Seh, J. Kibsgaard, C. F. Dickens, I. Chorkendorff, J. K. Nørskov and T. F. Jaramillo, *Science (80-.).*, 2017, **355**, 146.

48 H. Zhou, F. Yu, Q. Zhu, J. Sun, F. Qin, L. Yu, J. Bao, Y. Yu, S. Chen and Z. Ren, *Energy Environ. Sci.*, 2018, **11**, 2858–2864.

49 T. Bhowmik, M. K. Kundu and S. Barman, *ACS Appl. Mater. Interfaces*, 2016, **8**, 28678–28688.

50 L. Å. Näslund, Á. S. Ingason, S. Holmin and J. Rosen, *J. Phys. Chem. C*, 2014, **118**, 15315–15323.

51 R. K. B. Karlsson, A. Cornell and L. G. M. Pettersson, *J. Phys. Chem. C*, 2016, **120**, 7094–7102.

52 T. Weber, M. J. S. Abb, O. Khalid, J. Pfrommer, F. Carla, R. Znaiguia, V. Vonk, A. Stierle and H. Over, *J. Phys. Chem. C*, 2019, **123**, 3979–3987.

53 K. Zhou, C. B. Han, C. Wang, Z. Wang, Q. Zhang, X. Ke, J. Liu and H. Wang, *Energy Environ. Sci.*, 2020, **13**, 3082–3092.

54 C. Lei, Y. Wang, Y. Hou, P. Liu, J. Yang, T. Zhang, X. Zhuang, M. Chen, B. Yang, L. Lei, C. Yuan, M. Qiu and X. Feng, *Energy Environ. Sci.*, 2019, **12**, 149–156.

55 Z. Pu, J. Zhao, I. S. Amiinu, W. Li, M. Wang, D. He and S. Mu, *Energy Environ. Sci.*, 2019, **12**, 952–957.

56 T. Ling, T. Zhang, B. Ge, L. Han, L. Zheng, F. Lin, Z. Xu, W. Bin Hu, X. W. Du, K. Davey and S. Z. Qiao, *Adv. Mater.*, 2019, **31**, 1–7.

57 X. Huang, X. Xu, C. Li, D. Wu, D. Cheng and D. Cao, *Adv. Energy Mater.*, 2019, **9**, 1–10.

58 L. Yu, L. Wu, S. Song, B. McElhenny, F. Zhang, S. Chen and Z. Ren, *ACS Energy Lett.*, 2020, **5**, 2681–2689.

59 E. Demir, S. Akbayrak, A. M. Önal and S. Özkar, *ACS Appl. Mater. Interfaces*, 2018, **10**, 6299–6308.

60 F. Yang, Y. Zhao, Y. Du, Y. Chen, G. Cheng, S. Chen and W. Luo, *Adv. Energy Mater.*, 2018, **8**, 1–7.

61 J. Chen, J. Liu, J.-Q. Xie, H. Ye, X.-Z. Fu, R. Sun and C.-P. Wong, *Nano Energy*, 2019, **56**, 225–233.

62 Y. Yao, S. Hu, W. Chen, Z.-Q. Huang, W. Wei, T. Yao, R. Liu, K. Zang, X. Wang, G. Wu, W. Yuan, T. Yuan, B. Zhu, W. Liu, Z. Li, D. He, Z. Xue, Y. Wang, X. Zheng, J. Dong, C.-R. Chang, Y. Chen, X. Hong, J. Luo, S. Wei, W.-X. Li, P. Strasser, Y. Wu and Y. Li, *Nat. Catal.*, 2019, **2**, 304–313.

63 G. Yilmaz, C. F. Tan, Y. F. Lim and G. W. Ho, *Adv. Energy Mater.*, 2019, **9**, 1802983.

64 Y. Dang, J. He, T. Wu, L. Yu, P. Kerns, L. Wen, J. Ouyang and S. L. Suib, *ACS Appl. Mater. Interfaces*, 2019, **11**, 29879–29887.

65 H. Over, *Chem. Rev.*, 2012, **112**, 3356–3426.

66 A. Oh, H. Y. Kim, H. Baik, B. Kim, N. K. Chaudhari, S. H. Joo and K. Lee, *Adv. Mater.*, 2018, **1805546**, 1–8.

67 B. Weng, C. R. Grice, W. Meng, L. Guan, F. Xu, Y. Yu, C. Wang, D. Zhao and Y. Yan, *ACS Energy Lett.*, 2018, **3**, 1434–1442.

68 H. Jin, X. Liu, A. Vasileff, Y. Jiao, Y. Zhao, Y. Zheng and S.-Z. Qiao, *ACS Nano*, 2018, **12**, 12761–12769.

69 Y. Y. Ma, C. X. Wu, X. J. Feng, H. Q. Tan, L. K. Yan, Y. Liu, Z. H. Kang, E. B. Wang and Y. G. Li, *Energy Environ. Sci.*, 2017, **10**, 788–798.

70 G.Kresse and J.Furthmuller, *J. Phys. Chem. A*, 1996, **54**, 169–186.

71 G. Kresse and J. Hafner, *Phys. Rev. B*, 1993, **47**, 558–561.

72 G.Kresse and D.Joubert, *Phys. Rev. B - Condens. Matter Mater. Phys.*, 1999, **59**, 1758–1775.

73 J. P. Perdew, K. Burke and M. Ernzerhof, *Phys. Rev. Lett.*, 1996, **77**, 3865–3868.